

Numerical Heat Transfer, Part A: Applications



ISSN: 1040-7782 (Print) 1521-0634 (Online) Journal homepage: http://www.tandfonline.com/loi/unht20

Natural-Convection Heat Transfer in Channels with Isothermally Heated Convex Surfaces

I. Lakkis & F. Moukalled

To cite this article: I. Lakkis & F. Moukalled (2008) Natural-Convection Heat Transfer in Channels with Isothermally Heated Convex Surfaces, Numerical Heat Transfer, Part A: Applications, 53:11, 1176-1194, DOI: 10.1080/10407780701852985

To link to this article: http://dx.doi.org/10.1080/10407780701852985

	Published online: 04 Feb 2008.
	Submit your article to this journal 🗗
ılıl	Article views: 91
a a	View related articles 🗷
4	Citing articles: 11 View citing articles 🗹

Full Terms & Conditions of access and use can be found at http://www.tandfonline.com/action/journalInformation?journalCode=unht20

Numerical Heat Transfer, Part A, 53: 1176-1194, 2008

Copyright © Taylor & Francis Group, LLC ISSN: 1040-7782 print/1521-0634 online DOI: 10.1080/10407780701852985



NATURAL-CONVECTION HEAT TRANSFER IN CHANNELS WITH ISOTHERMALLY HEATED CONVEX SURFACES

I. Lakkis and F. Moukalled

Department of Mechanical Engineering, American University of Beirut, Beirut, Lebanon

This article reports on a numerical investigation conducted to study laminar natural-convection heat transfer in channels with convex surfaces that are isothermally heated. Six Grashof number (Gr) values ($10 \le \text{Gr} \le 10^4$) and 11 radii of curvature ($1 \le \kappa \le \infty$) are considered. The results are displayed in terms of streamline and isotherm plots, centerline pressure profiles, inlet mass flow rates, and local and average Nusselt number estimates. At the lowest radius of curvature ($\kappa = 1$), computations reveal the formation of recirculation zones in the exit section for all values of Grashof number considered. As the radius of curvature increases, the Gr value at which recirculation occurs also increases, until it disappears at κ values greater than 1.5. For all configurations studied, the average Nusselt number ($\overline{\text{Nu}}$) results indicate an increase in heat transfer with increasing Grashof number values. Moreover, the value of κ at which ($\overline{\text{Nu}}$) peaks increases with increasing Gr. Inlet volume flow rate and average Nusselt number correlations are presented.

INTRODUCTION

Many engineering applications involve natural-convection flow in passages bounded by curved surfaces. Examples include flow in chimneys, cooling of electronic equipment, and energy conservation in buildings aiming to optimize heat transfer using innovative designs and architecture. However, most of the studies reported have been confined to natural-convection heat transfer in rectangular channels and pipes. Natural convection in channels with curved entry surfaces has not yet been seriously examined and therefore represents the focus of the present investigation. The geometry selected for this study is a generic configuration (not specific to any application) of a channel with convex heated walls (see Figure 1a). The flow and heat transfer in such configurations are expected to be more complex than their counterparts in straight vertical channels and pipes, because of changes in the flow cross-sectional area and the potential for flow separation.

Several experimental and numerical investigations of natural-convection heat transfer in straight vertical channels have been reported in the literature. Initial numerical solutions employed a parabolic model [1, 2] of the conservation equations because of the difficulty of implementing the inlet boundary condition in a full elliptic

Received 6 July 2007; accepted 27 November 2007.

Address correspondence to F. Moukalled, Department of Mechanical Engineering, American University of Beirut, P.O. Box 11-0236, Riad El Solh, Beirut 1107 2020, Lebanon. E-mail: memouk@aub.edu.lb

NOMENCLATURE							
c_p g Gr h H	specific heat gravitational acceleration Grashof number $[=g\beta\rho^2(T_w-T_\infty)w^3/\mu^2]$ convection heat transfer coefficient height of curved channel section and of channel extension fluid thermal conductivity dimensionless length of hot wall	$\begin{array}{c} \mathbf{s} \\ T \\ T_w \\ T_{\infty} \\ u, v \\ U, V \\ w \\ x, y \\ X, Y \end{array}$	surface vector dimensional temperature dimensional wall temperature dimensional inlet temperature dimensionless velocity components dimensional velocity components channel inlet width dimensionless coordinates dimensional coordinates				
Nu Nu	local Nusselt number average Nusselt number	β	thermal expansion coefficient dimensionless temperature				
p	dimensionless pressure	К	dimensionless radius of curvature				
P Pr R	dimensional pressure Prandtl number $(=\mu c_p/k)$ radius of curvature	μ ρ	dynamic viscosity density				

model [3–5]. Later developments in numerical techniques alleviated this constraint, thereby allowing accurate predictions using the full Navier-Stokes equations.

An early numerical study of natural-convection heat transfer in straight vertical channels with isothermal walls was conducted by Bodoia and Oesterle [1] using a

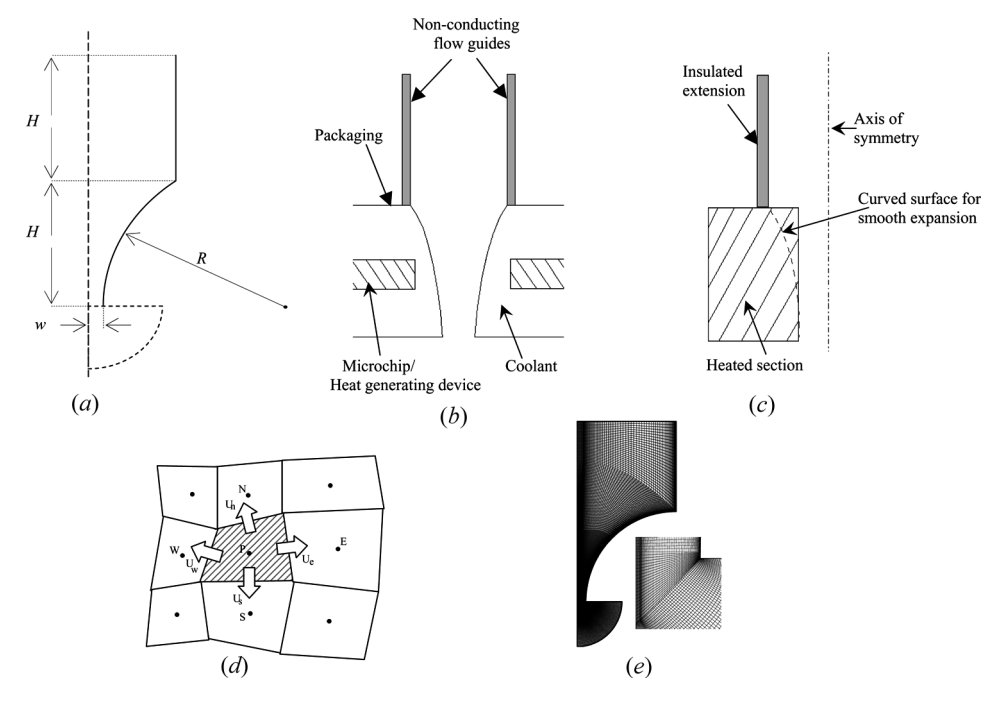


Figure 1. (a) Computational domain. (b) Physical domain. (c) Configuration studied by Manca et al. [16]. (d) A typical control volume. (e) Grid network for $\kappa = 1$.

parabolic model. The Nusselt numbers calculated were in close agreement with results obtained by Elenbaas [6]. Using the same parabolic model, Aung et al. [2] reported results in the same geometry for both isothermal and prescribed heat flux wall boundary conditions. Experiments were also performed to validate the numerical results. Sparrow et al. [7] analyzed the natural-convection flow in straight vertical channels with one isothermal wall and one insulated wall.

Naylor et al. [3] presented a numerical study for steady two-dimensional laminar free-convection flow between parallel isothermal plates including entrance effects by solving the full elliptic forms of the Navier-Stokes and energy equations. Their work included a novel technique for handling inflow boundary conditions that simulates the induced flow more realistically. Maliska and Marcondes [4] employed an elliptic formulation to solve for natural-convection flow in vertical channels and reported flow reversal at the exit. Marcondes and Maliska [5] studied numerically the natural convection heat transfer in straight and L-shaped channels, using an elliptic solver, and proposed a method for the application of boundary conditions at the channel inlet. Nieckle and Azevedo [8] reported experimental and numerical results, with the numerical results obtained using parabolic and elliptic procedures, on natural-convection in a channel with one wall at a prescribed temperature and one wall insulated. Haaland and Sparrow [9] analyzed numerically the natural convection in a vertical channel with a point source and a distributed heat source placed at the inlet section.

Several investigations were also carried out in channels with downstream adiabatic or unheated extensions, which have been referred to in the literature as the channel-chimney systems. Straatman et al. [10] reported on an experimental investigation, using a Mac-Zehnder interferometer, of natural convection in a straight channel with isothermal walls. Measurements validating the numerical heat transfer results showed a substantial increase in heat transfer rates due to the chimney effects. A correlation of average values of Nusselt number in terms of values of channel Rayleigh number, expansion ratio, and extension ratio was proposed. Fisher and Torrance [11] studied experimentally the natural convection in a vertical channelchimney system with a heat sink. Experimental investigations to study the effect of adding adiabatic extensions downstream from a vertical channel heated with a constant heat flux, either symmetrically or asymmetrically, were carried out by Auletta et al. [12] and by Manca et al. [13], respectively. The measured wall temperature profiles in [12] revealed that optimal enhancement in heat transfer is obtained in insulated extensions that are about three times the channel height and for an expansion ratio of around 2 for all configurations. Results reported in [13] indicate better system performance with a larger chimney.

Manca et al. [14] reported experimental results of natural convection of air in a symmetrically and asymmetrically heated vertical channel with an adiabatic extension and showed the effect of the heating mode on the interaction of the hot plume rising from the channel, the cold inflow, and the vortex region in the chimney corner. Alutta and Manca [15] reported on the effect of the geometric parameters (expansion and extension ratios) on the buoyancy-driven flow in symmetrically heated vertical channel—chimney systems and presented correlations for local Nusselt number values. Manca et al. [16] carried out an experimental investigation in an asymmetrically heated vertical channel, with a uniform heat flux

boundary condition and downstream unheated parallel extensions. The results reported indicated that for the largest height-to-width ratio, the adiabatic extensions improved the thermal performance in terms of lowering the maximum wall temperature of the channel.

Pop and Takhar [17] and Magyari et al. [18] analyzed the free-convective flow over a heated two-dimensional curved surface. Nakayama et al. [19] and Char and Chang [20] considered the same problem for the situation where the heated curved surface is embedded in a fluid-saturated porous medium and in a micropolar fluid, respectively. These studies demonstrated the existence of a family of curved surfaces and of corresponding temperature distributions, which permit similarity solutions of power-law type. The equation of the corresponding shape curves was expressed either in terms of a series expansion [17, 19] or in terms of Gauss's hypergeometric function [18].

The configuration selected for the current investigation (Figure 1a) is the one that was used by Moukalled et al. [21, 22] in their study of mixed-convection heat transfer in channels with a heated curved surface bounded by a vertical adiabatic wall. The curved wall could represent the sides of a shell enclosing a computer chip, or a heat-generating device, submerged in liquid to enhance cooling (Figure 1b), and the extensions are used to guide the flow and/or to prevent the hot fluid from flowing over other sensitive devices. The same configuration could also be seen as a variation of the work reported by Manca et al. [16] whereby, to increase heat transfer, an expansion of the channel was suggested (Figure 1c), with the expansion being sudden. In this work a smooth expansion to the desired level is suggested.

PHYSICAL MODEL AND GOVERNING EQUATIONS

Figure 1a illustrates schematically the physical situation considered in this study. As a result of the symmetry, only half of the channel is considered. The curved wall constitutes part of a circle with radius R. This part is maintained at a uniform temperature T_w that is higher than the surrounding fluid temperature T_∞ . The temperature gradient creates density variations within the fluid and gives rise to the buoyancy forces that drive the flow. The upper vertical section of the wall is assumed to be insulated. The working fluid is selected to be air and enters the channel from the bottom.

The equations governing the flow and heat transfer are those expressing the conservation of mass, momentum, and energy. The flow is assumed to be laminar, steady, and two-dimensional with constant fluid properties, except for the variations induced in the body-force term. The transport equations are nondimensionalized using the following dimensionless variables:

$$x = \frac{X}{w} y = \frac{Y}{w} \kappa = \frac{R/w}{H/w} u = \frac{\rho U w}{\mu \, Gr^{1/2}}$$

$$v = \frac{\rho V w}{\mu \, Gr^{1/2}} p = \frac{\rho P w^2}{\mu^2 \, Gr^{1/2}} \theta = \frac{T - T_{\infty}}{T_w - T_{\infty}}$$
 (1)

With the above-stated assumptions and using the Boussinesq approximation, the dimensionless equations governing transport of mass, momentum, and energy are written respectively as

$$\nabla \cdot \mathbf{u} = 0 \tag{2}$$

$$Gr^{1/2}(\mathbf{u}\cdot\nabla u) = -\mathbf{i}\cdot\nabla p + \nabla\cdot\nabla u \tag{3}$$

$$Gr^{1/2}(\mathbf{u} \cdot \nabla \mathbf{v}) = -\mathbf{j} \cdot \nabla p + \nabla \cdot \nabla \mathbf{v} + Gr^{1/2}\theta \tag{4}$$

$$Gr^{1/2}(\mathbf{u}\cdot\nabla\theta) = \frac{1}{\mathbf{Pr}}\nabla\cdot\nabla\theta \tag{5}$$

The boundary conditions used are

$$\frac{\partial u}{\partial y} = \frac{\partial v}{\partial y} = 0 \qquad p = p_{\infty} = 0 \qquad \begin{cases} \frac{\partial \theta}{\partial y} = 0 & \text{if } v \ge 0 \\ \theta = 0 & \text{if } v < 0 \end{cases} \qquad y = 2H \qquad (6)$$

$$\frac{\partial u}{\partial x} = \frac{\partial v}{\partial x} = \frac{\partial \theta}{\partial x} = 0 \qquad x = 0 \tag{7}$$

$$u = v = \frac{\partial \theta}{\partial x} = 0$$
 $x = 1 + \kappa - \sqrt{\kappa^2 - H^2}$ $H \le y \le 2H$ (8)

$$u = v = 0$$
 $\theta = 1$ $1 \le x \le 1 + \kappa - \sqrt{\kappa^2 - H^2}$ $0 \le y \le H$ (9)

The methodology for the inlet boundary condition proposed by Naylor et al. [3] is adopted. For that purpose, the domain is extended as shown by the dotted line in Figure 1a and, at the inlet to the extended section, a Jeffrey-Hamel flow is assumed (for more details, the reader is referred to Batchelor [23]). Physically, the flow at the extended circular boundary is assumed to be normal at the boundary and directed toward the center point O in Figure 1a. In addition, if this boundary is placed far enough from the heated wall, the temperature can be assumed to be equal to the surrounding fluid temperature T_{∞} and the radial stress can be set to zero. Mathematically this is expressed as

$$\mathbf{u} \cdot \mathbf{t} = -p + 2\nabla \mathbf{u} \cdot \mathbf{n} = \theta = 0 \qquad 0 \le x \le 5 \qquad -5 \le y \le 0 \tag{10}$$

where \mathbf{n} and \mathbf{t} are unit vectors in the direction normal and tangential to the surface, respectively.

After calculating the velocity and temperature fields, the local and average Nusselt numbers along the hot curved wall are calculated as

$$Nu = \frac{hw}{k} \qquad \overline{Nu} = \frac{1}{\ell} \int_{0}^{\ell} Nu \, d\ell \tag{11}$$

where w is the width of the channel at the inlet. Moreover, the heat transfer coefficient h is defined as

$$h = \frac{k}{w} (\nabla \theta \cdot \mathbf{n})_{\text{wall}} \Rightarrow \text{Nu} = (\nabla \theta \cdot \mathbf{n})_{\text{wall}}$$
(12)

Another parameter of interest in this study is the dimensionless volume flow rate Q (for half the channel), which is calculated at the inlet to the channel as

$$Q = \int_{\mathbf{S}} \mathbf{u} \cdot d\mathbf{s} \tag{13}$$

SOLUTION PROCEDURE

The system of coupled conservation equations [Eqs. (2)–(5)], subject to the stated boundary conditions [Eqs. (6)–(10)] is solved numerically using a collocated finite-volume method (FVM). Checkerboard pressure and velocity fields are eliminated through the use of the momentum-weighted interpolation method (MWIM) for the calculation of the mass fluxes across the control-volume faces [24]. The unknown pressure field is obtained using the SIMPLE algorithm of Patankar [25–27]. Solutions are generated by subdividing the physical space into a number of control volumes with grid points placed at their geometric centers (Figure 1d). The discretized equations are derived by integrating the conservation equations over a control volume (Figure 1d) and then transforming the integrated equations into algebraic ones by expressing the variation in the dependent variable and its derivatives in terms of the grid-point values. The diffusion flux is discretized along each surface of the control volume using the method described by Zwart et al. [28], while the convective flux is calculated using the third-order SMART scheme [29] applied within the context of the NVSF methodology [30]. In addition, the integral value of the source term over the control volume P (Figure 1d) is evaluated by assuming the source at the control-volume center to be equal to the mean value over the whole control volume. The set of algebraic equations is then solved iteratively using the tri-diagonal matrix algorithm (TDMA) [25]. All computations are performed using nonuniform grids with denser clustering near the walls, where boundary layers develop and high gradients are expected. Grid networks (Figure 1e) are generated using the algebraic transfinite interpolation technique [31].

Numerical Accuracy and Validation

To investigate the sensitivity of the solution to the grid used, solutions in some selected cases were obtained on successively finer grids and the predicted mass flow rates and average Nusselt numbers were compared. A final nonuniform mesh of size 25,830 grid points was used to generate all results presented in this article. The grid points were concentrated close to solid boundaries, where large gradients are expected (Figure 1c). The accuracy of the calculations was verified by comparing computed profiles of velocity, temperature, and local Nusselt number using the 25,830 nonuniform grid with those obtained on a 57,600 nearly uniform grid.

Source	Number of nodes	Inlet domain radius	$\overline{\mathrm{Nu}}$	Q
Naylor et al. [3]	8,465	3	2.4055	2.084
Naylor et al. [3]	9,249	4	2.4046	2.076
Naylor et al. [3]	10,033	5	2.4040	2.073
Naylor et al. [3]	14,369	5	2.4046	2.073
Current	$30 \times 383 = 11,490$	5	2.4162	2.049
Current	$45 \times 574 = 25,830$	5	2.4059	2.053

Table 1. Comparison between present numerical results and those of [3] for natural-convection in a straight channel at a Grashof number of 10^4

The maximum difference of the various quantities predicted was smaller than 0.01%. Conservation of the various physical quantities was satisfied to within $10^{-6}\%$ in each control volume. As a further check for accuracy, solutions in a vertical channel were compared against similar ones reported by Naylor et al. [3] at a Grashof number of 10^4 and are presented in Table 1 and Figure 2. As shown in Table 1, the differences in the average Nusselt number and the volume flow rate between the two solutions are 0.054% and 0.965%, respectively. Moreover, the local Nusselt number distributions generated using two different grids are indistinguishable, fall on top of numerical predictions reported in [3], and are in close agreement with experimental measurements presented by Wirtz and Haag [32].

RESULTS AND DISCUSSION

The governing parameters in the problem are the Prandtl number (Pr), the Grashof number (Gr), and the channel radius of curvature (κ). Results are obtained

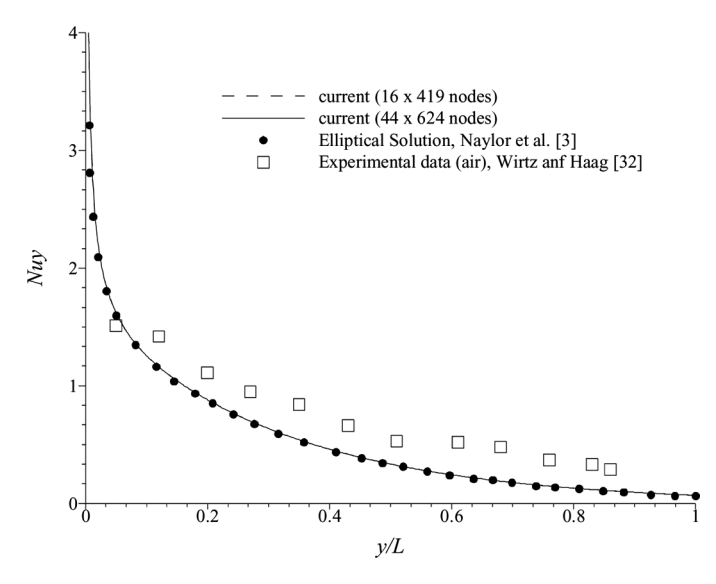


Figure 2. Comparison of local Nusselt number variation with the numerical data of Naylor et al. [3] and experimental data of Wirtz and Haag [32].

for 11 radii of curvature ($\kappa = 1$, 1.1, 1.2, 1.3, 1.4, 1.5, 2, 5, 20, 50, and ∞) and six Grashof number values (Gr = 10, 10^2 , 5×10^2 , 10^3 , 5×10^3 , and 10^4). Moreover, the working fluid selected is air and the Prandtl number is assigned a value of 0.7.

Results are presented in the form of streamlines, isotherms, centerline pressure, mass flow rate estimates, and local and average Nusselt number values.

Streamlines and Isotherms

Representative streamline and isotherm plots are displayed in Figures 3–7. Figures 3–5 show the effects on the velocity and temperature fields of varying values of Grashof number holding the curvature constant, while Figures 6 and 7 reveal the influence of curvature on the flow and heat transfer characteristics at a given Grashof number. Above each configuration, the minimum contour value, the uniform increment between any two contours, and the maximum contour value are displayed. On some of the streamline maps, additional streamlines are included to better visualize the flow, and the corresponding values of the stream function are displayed on the plots.

Figure 3 presents results for the case in which the curved wall is a quarter of a circle (i.e., $\kappa = 1$). This radius of curvature results in an expansion ratio of 1:10 (i.e., ratio of outlet to inlet areas), which is the largest studied in this work. At all values of Grashof number, two recirculation zones in the upper half of the domain (exit section) occur. At values of Grashof number less than 10^3 , most of the flow entering

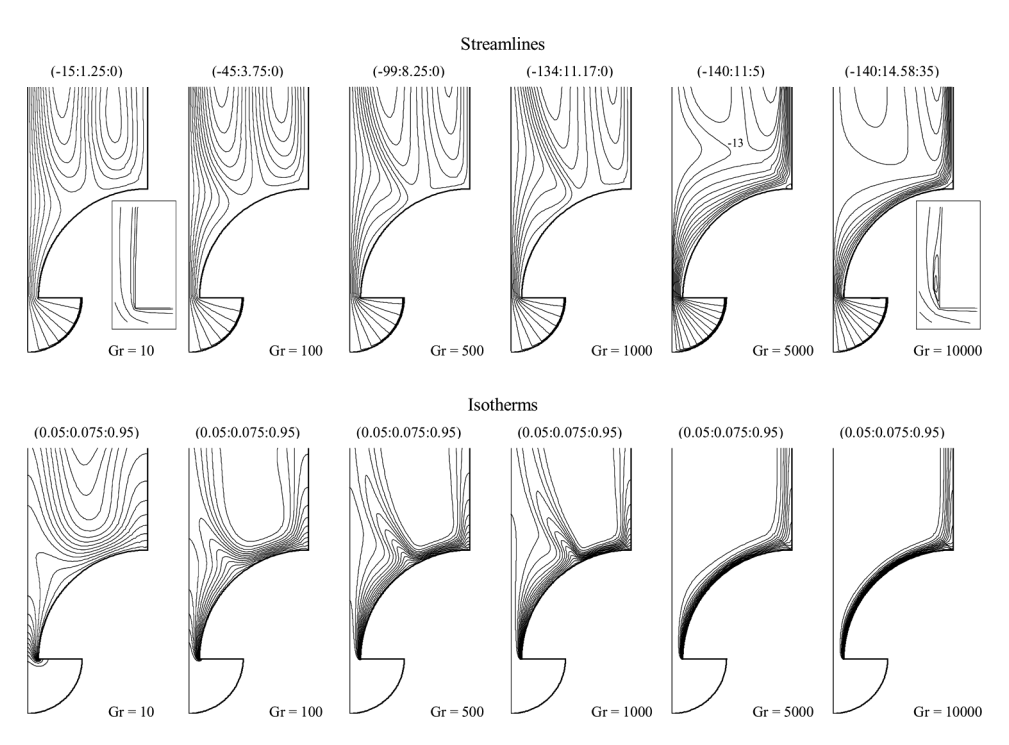


Figure 3. Streamlines (upper) and isotherms (lower) for various values of Gr with $\kappa = 1$.

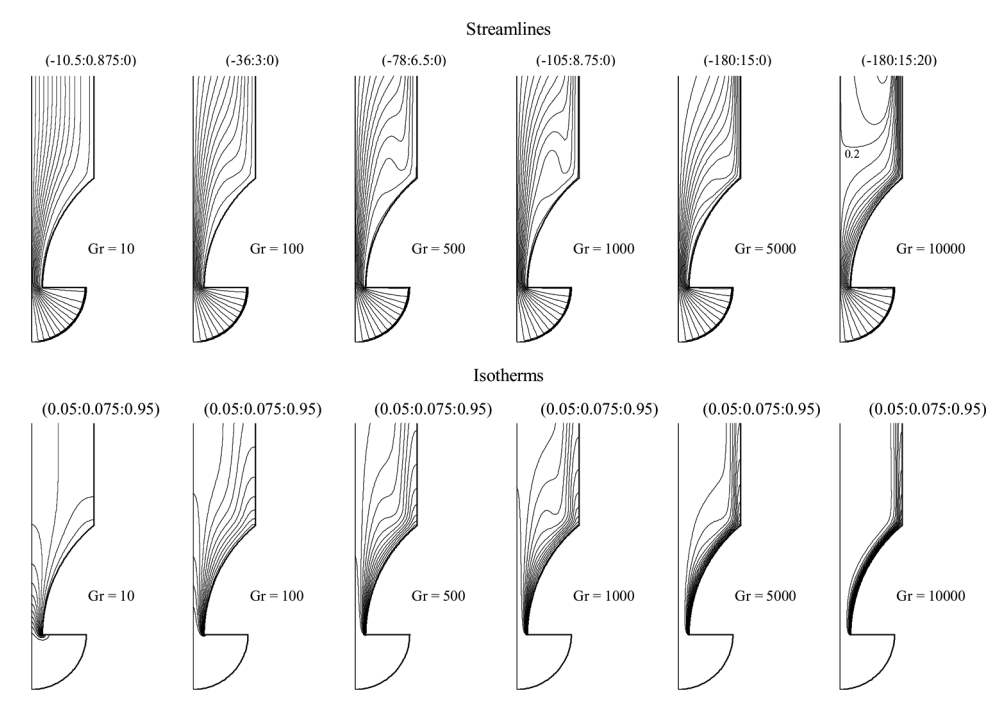


Figure 4. Streamlines (upper) and isotherms (lower) for various values of Gr with $\kappa = 1.3$.

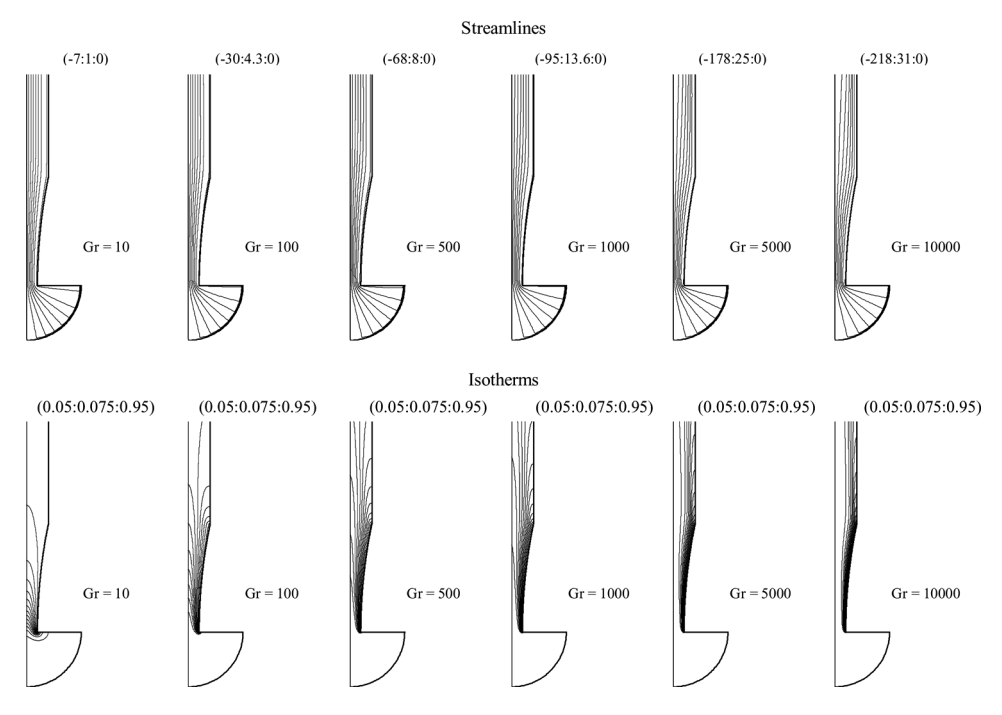


Figure 5. Streamlines (upper) and isotherms (lower) for various values of Gr with $\kappa = 5$.

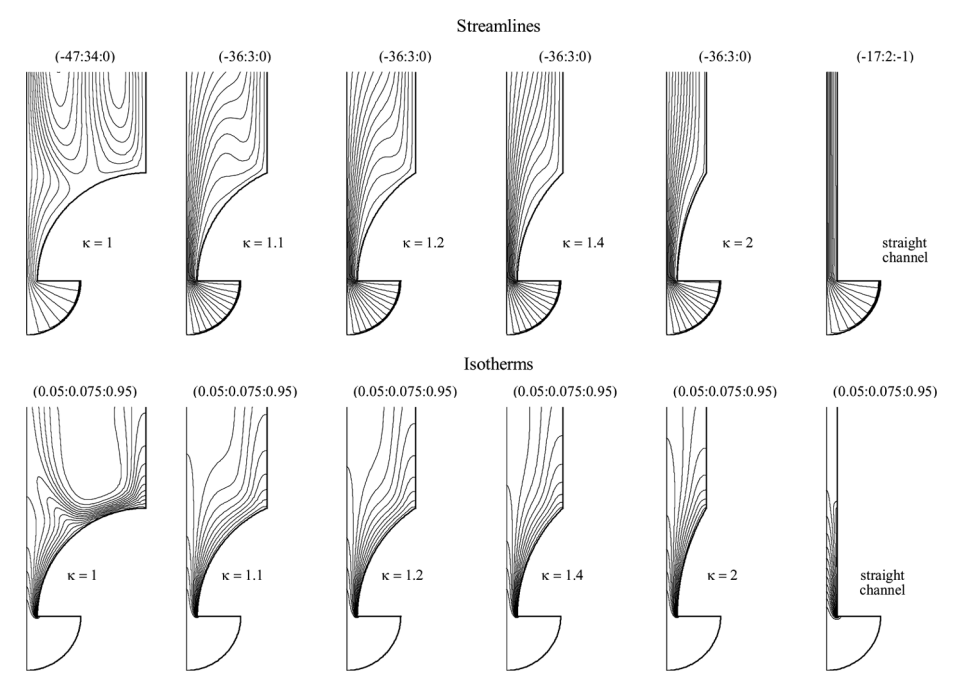


Figure 6. Streamlines (upper) and isotherms (lower) for various values of κ with $Gr = 10^2$.

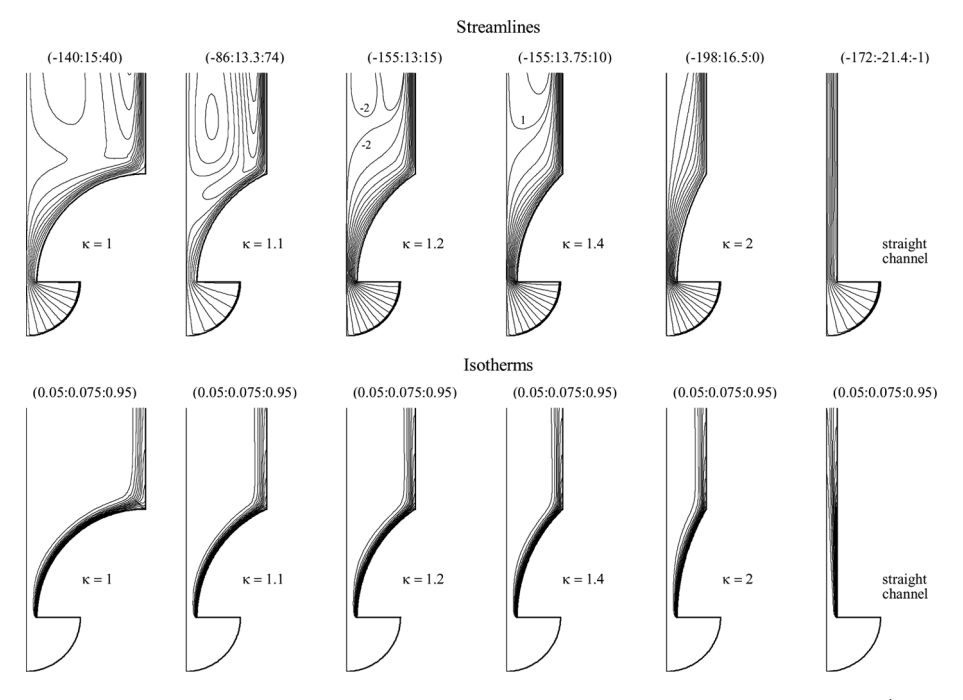


Figure 7. Streamlines (upper) and isotherms (lower) for various values of κ with $Gr = 10^4$.

the domain from the bottom separates and leaves the domain without moving over the entire length of the curved surface. The distance along the curved wall at which separation occurs increases with increased values of Grashof number. This behavior is due to the fact that at low Grashof number values, buoyancy effects are relatively low and cannot overcome the adverse pressure gradient along the curved surface caused by the increase in the channel cross-sectional area. At high values of Grashof number ($\geq 5 \times 10^3$), buoyancy effects become strong enough for the flow in the lower half of the domain to overcome the retarding pressure gradient effects and consequently the flow moves over the entire curved wall without separating. For these reasons, the bulk of the flow entering the domain leaves the channel along the central portion for Grashof number values $\leq 10^3$ and along its insulated wall for $Gr \geq 5 \times 10^3$. For Gr = 10 and 10^4 , a small plot magnifying the inlet region to the channel is presented. As depicted in Figure 3, no recirculation is noticed when Gr = 10, while a recirculation zone is formed at $Gr = 10^4$, which is in accord with predictions reported by Naylor et al. [3] for natural convection in a vertical channel.

Isotherms displayed in Figure 3 reflect the behavior described above. At Gr=10, isotherms are uniformly distributed over the domain, indicating dominant conduction heat transfer mode. This is further revealed by the preheating of the fluid entering the domain at ambient temperature, evidenced by the diffusion of heat upstream from the heated section. As Gr increases, upstream diffusion decreases and isotherms become more clustered, indicating stronger convection effects. For $Gr \le 10^3$, temperature contours imitate the flow field, with the recirculation zones in the exit section clearly reflected in the distribution of isotherms. As shown in Figure 3, the temperature of the cold fluid entering the domain from the top increases while moving downward and results in the temperature distribution displayed. For $Gr \ge 5 \times 10^3$, isotherms are condensed along the hot curved surface and the insulated vertical wall of the channel, which indicates that most of the fluid entering the domain from the bottom remains close to the wall until leaving the channel. As expected, the densest clustering of isotherms is obtained at the highest Gr value (i.e., $Gr = 10^4$).

Figure 4 displays results for $\kappa=1.3$. For this configuration, the expansion ratio of the curved section is around 5.7. For $\text{Gr} \leq 5 \times 10^3$, the streamlines presented in the figure do not reveal any recirculation at the exit, indicating that buoyancy forces overcome the hydrodynamic effects, which result from the pressure increase due to gradual expansion in the channel. Moreover the buoyancy-entrained flow is discharged through the entire channel cross section. For Gr=10, the streamlines follow the contour of the channel. As Gr increases, the velocity of the fluid in the vicinity of the channel walls increases. For continuity to be satisfied, this near-wall increase in velocity is associated with a decrease in velocity away from the wall. As a result, the streamlines show that the flow drifts toward the channel wall. As Gr increases to 10^4 , the acceleration of the flow in the vicinity of the wall causes most of the fluid induced by buoyancy to be discharged along the channel wall and consequently causes the formation of a recirculation zone in the exit section of the channel.

The thermodynamic characteristics of the flow can be inferred from the isotherms presented in Figure 4. At Gr=10, the isotherms are uniformly distributed and the upstream diffusion is considerable, which indicates that conduction is the

dominant heat transfer mode. As Gr increases, isotherms become more distorted, which indicates a higher contribution of convection to the total heat transfer. The denser clustering of isotherms along the channel wall reveals this in more detail.

Results presented in Figure 5 are for a channel with an expansion ratio ≈ 2 ($\kappa = 5$). For this configuration, the rate of expansion is small and the effects of adverse pressure gradient over the curved surface are smaller than the buoyancy effects at all values of Grashof number, consequently no recirculation exists in all cases studied. The isotherms of Figure 5 indicate that conduction is dominant at low Gr values, with convection effects increasing with increased values of Grashof number. The tendency of the fluid to flow close to the hot walls for large values of Gr is confirmed by the isotherm maps, which show behavior similar to the cases discussed earlier.

The effects of the hot-wall curvature on the hydrodynamic and thermal fields are depicted in Figures 6 and 7 for Gr values of 10² and 10⁴, respectively. For $Gr = 10^2$ (Figure 6), recirculation in the exit section occurs at the highest expansion value (i.e., the lowest radius of curvature, $\kappa = 1$). For lower expansion ratios (i.e., $\kappa > 1$), the decrease in the adverse pressure gradient allows the flow to follow the contour of the curved section more closely, as indicated by the streamlines displayed. This is further confirmed by the isotherms presented in the figure, where the effect of recirculation for $\kappa = 1$ is obvious. However, for this Gr value, convection effects are low, as revealed by the uniform spread of isotherms over the domain and the upstream diffusion of heat at the inlet to the heated channel section. For $Gr = 10^4$, the streamline maps displayed in Figure 7 show the formation of recirculation zones in the exit section of channels for which $\kappa < 1.4$. However, most of the buoyancy-induced flow entering the domain from the bottom section moves in the vicinity of the wall until it is discharged, indicating that there are strong convection effects. As shown, the size of the recirculation decreases with increasing κ for the reasons stated above, until it fades away at $\kappa > 2$. The strength of convection heat transfer manifests itself by the dense clustering of isotherms close to the hot surface. Packing of isotherms decreases as the fluid moves along the hot wall (showing boundary-layer behavior); the decrease is higher at lower κ values because of the longer distance the fluid has to travel.

An important hydrodynamic parameter is the buoyancy-induced volume flow rate. Volume flow rate values have been calculated at the inlet to the channel using Eq. (13). To give the actual relative strength at different Grashof numbers, the volume flow rates obtained by Eq. (13) have been multiplied by $Gr^{1/2}$. The results are presented in Table 2. At all κ values, the buoyancy-induced volume flow rate increases with increasing Gr values from 10 up to 5×10^3 . This increase is due to the increase in buoyancy, which accelerates the flow along the curved hot wall. When $Gr=10^4$, a decrease in the volume flow rate, as compared to values obtained at $Gr\le 5\times 10^3$, is noticed for values of $\kappa\le 1.4$, while it continues to increase for values of $\kappa>1.4$. This behavior is credited to the combined effects of channel curvature and buoyancy forces on the pressure. As the Grashof number increases, the velocity increases, resulting in a decrease in pressure. Moreover, the expansion of the channel results in an additional decrease in pressure. For the induced flow to exit the channel, its static pressure should be at least equal to the atmospheric pressure. For this increase to take place, the flow adjusts itself by increasing the size of the recirculation

	Gr					
К	10	100	500	1,000	5,000	10,000
1	7.85	25.19	60.47	84.91	139.90	140.50
1.1	7.69	36.74	77.53	104.48	180.55	86.74
1.2	10.76	36.90	77.93	105.25	181.64	162.95
1.3	10.61	36.98	78.29	105.59	181.64	152.68
1.4	10.45	37.00	78.58	105.84	181.50	159.60
1.5	10.31	36.97	78.83	106.12	182.54	191.78
2	9.65	36.22	78.97	105.71	178.66	198.14
5	7.09	30.13	68.97	95.49	178.01	217.86
20	4.27	21.98	51.76	72.67	149.46	194.69
50	3.53	19.51	46.83	65.90	137.94	182.82
Straight channel	3.01	17.65	43.18	60.92	128.74	172.56

Table 2. Volume flow rate at the inlet section of the channel $(Q \operatorname{Gr}^{1/2})$

zone deeper inside the domain, which results in a decrease in the buoyancy-induced volume flow rate. For the same reason, there exists at any Grashof number a κ value for which the mass flow rate is maximized; this value generally increases as Grashof number increases.

For $10^2 \le \text{Gr} \le 5 \times 10^3$, $Q \, \text{Gr}^{1/2}$ values presented in Table 2 are correlated with a maximum absolute error less than 4.15% via the following equation:

$$Q \operatorname{Gr}^{1/2} = a + \frac{b}{\kappa} + \frac{c}{\kappa^3} + \frac{d}{\kappa^5} + \frac{e}{\kappa^7}$$
 (14)

where

$$a = 9.721 + 0.087123 \,\text{Gr} - 4 \times 10^{-5} \,\text{Gr}^2 + 5.51 \times 10^{-9} \,\text{Gr}^3$$

$$b = 45.388 + 0.25114 \,\text{Gr} - 1.3265 \times 10^{-4} \,\text{Gr}^2 + 1.81 \times 10^{-8} \,\text{Gr}^3$$

$$c = -129.707 - 0.71878 \,\text{Gr} + 3.5693 \times 10^{-4} \,\text{Gr}^2 - 4.88 \times 10^{-8} \,\text{Gr}^3$$

$$d = 219.576 + 0.99411 \,\text{Gr} - 4.7236 \times 10^{-4} \,\text{Gr}^2 + 6.48 \times 10^{-8} \,\text{Gr}^3$$

$$e = -130.982 - 0.49423 \,\text{Gr} + 2.3221 \times 10^{-4} \,\text{Gr}^2 - 3.22 \times 10^{-8} \,\text{Gr}^3$$

The above conclusions are confirmed by the pressure profile along the channel centerline presented in Figure 8. In Figure 8a, results for the highest channel expansion ratio ($\kappa=1$) are presented. The plots indicate an increase in pressure drop at the inlet to the channel as the Grashof number increases. The pressure gradually increases in the diverging section and remains almost constant in the exit section, where recirculation occurs. The rate of pressure increase in the diverging section is such that its value at exit from this section is nearly equal to its value at the channel exit for Grashof number $\leq 5 \times 10^3$. For $Gr = 10^4$, however, the rate of increase in pressure is faster, reaching the exit value at nearly x=5, and remains constant thereafter. This behavior is due to the larger recirculation zone, which penetrates deeper into the convex heated section of the channel, as explained earlier. For $\kappa=5$ (Figure 8b), because no recirculation occurs in the exit section, values of pressure at the inlet to

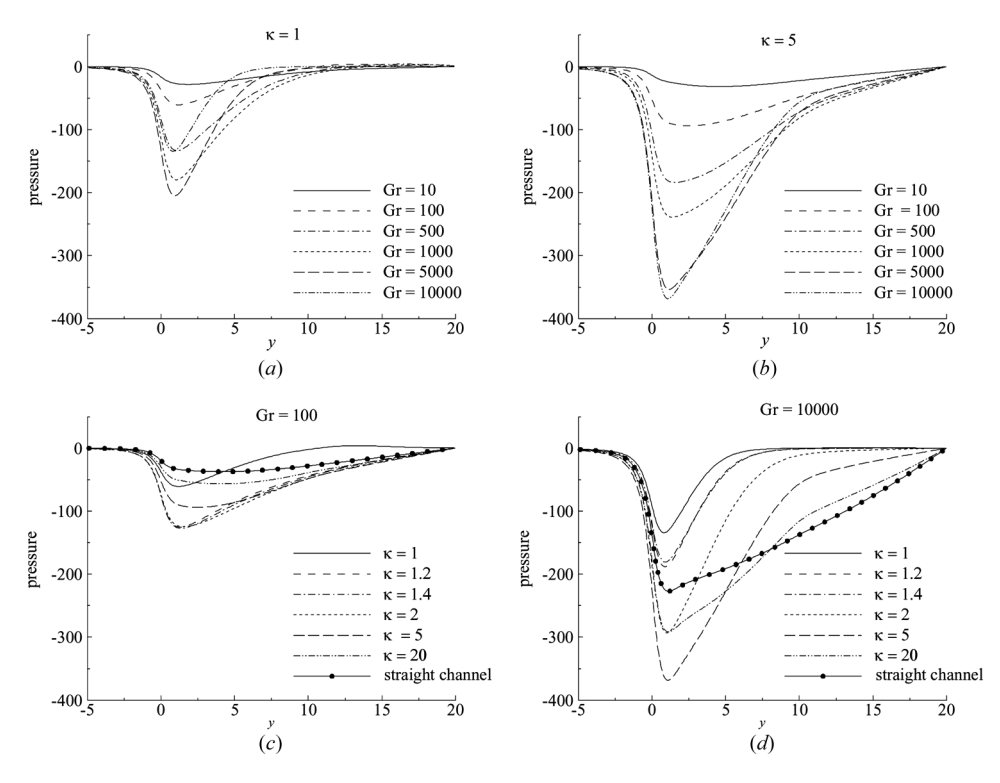


Figure 8. Centerline pressure variation with channel height (y).

the exit section are lower than values obtained for $\kappa=1$ and increase linearly in that section to the desired value at the exit. The effects of the hot-wall curvature on the centerline pressure profiles are displayed in Figures 8c and 8d for $Gr=10^2$ and 10^4 , respectively. At low Gr value (Figure 8c), convection effects are low and pressure variation is more dictated by the expansion ratio of the channel and consequently the size of the recirculation zone in the exit section. At low expansion ratios ($\kappa \ge 2$), the pressure drop at the inlet increases with decreasing κ until the size of the recirculation zone necessitates lower pressure drops at the inlet so that the pressure at the exit is equal to the atmospheric pressure. This occurs for the values of $\kappa < 2$. At $Gr = 10^4$ (Figure 8d), the same behavior is observed, with differences being clearer and the decrease in pressure drop at the inlet to the channel starting at a slightly higher κ value ($\kappa = 2$) because of stronger convection effects.

Nusselt Numbers

Typical local Nusselt number variations (Nu) along the hot wall of the channel are presented in Figure 9. Values are plotted as a function of their location along the vertical height of the curved section (y). The effects of buoyancy forces on Nusselt number distribution are displayed in Figures 9a and 9b for $\kappa = 1$ and 5, respectively. For both κ values, the Nusselt number level increases with increasing Gr number

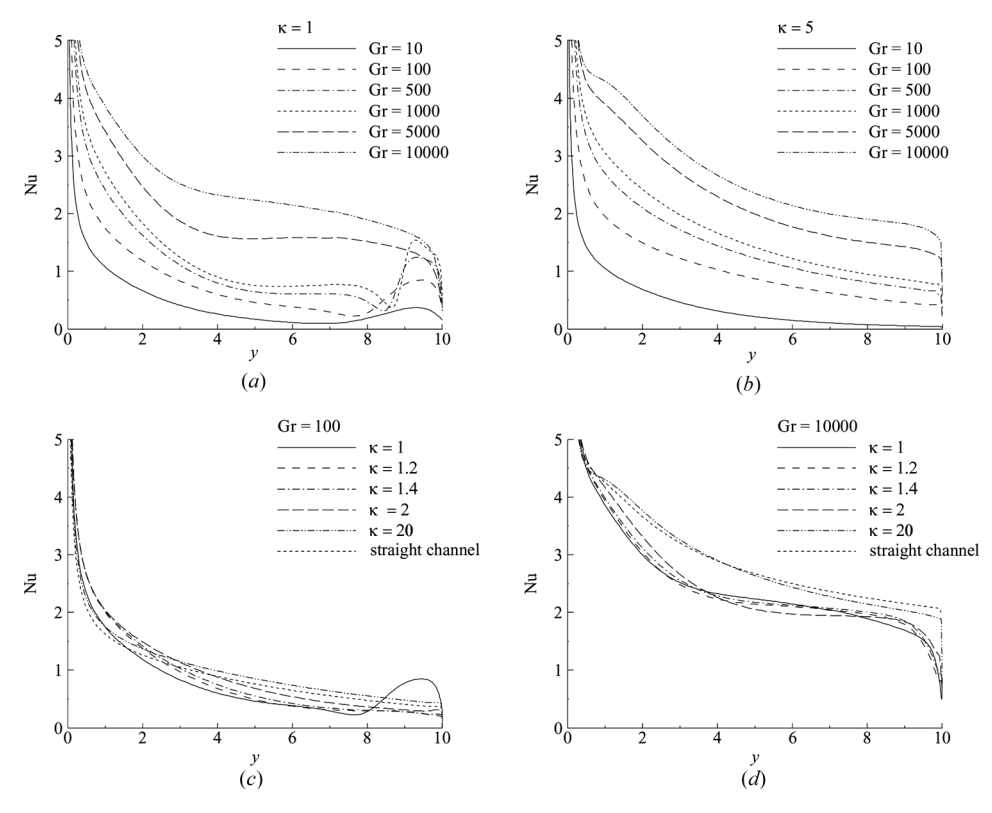


Figure 9. Nusselt number variation with channel height (y).

values, indicating stronger convection effects. At any Gr value, the Nusselt number decreases as the fluid moves over the curved section, because of the decreasing temperature difference between the fluid and the hot wall. For $\kappa = 1$, an increase in Nu is apparent at $Gr < 5 \times 10^3$ in the upper region of the hot wall (y > 8). This is the location where the descending recirculating cold fluid meets the hot wall, as revealed by the streamlines presented in Figure 3. This does not occur at high Gr values (for $\kappa = 1$) because recirculation moves away from the wall toward the centerline of the channel. The effects of the hot-wall convexity on the local Nusselt number values are displayed in Figures 9c and 9d for $Gr = 10^2$ and 10^4 , respectively. As κ varies at a given Gr value, the two parameters that control the variation of Nusselt number are the expansion ratio and the length of the hot wall. As the expansion ratio increases, the average velocity in the channel decreases. However, the velocity in the vicinity of the wall is also affected by recirculation that may form in the exit section. The formation of recirculation zones may cause the fluid to either accelerate and flow close to the wall, or separate from the wall and flow in the core region. In addition, if recirculation occurs and reaches the hot wall, it will enhance heat transfer and increase Nu. Therefore, channel expansion may either reduce or increase convection heat transfer. Similarly, an increase in the expansion ratio is associated with an increase in the length of the hot wall. Because the fluid is heated

	Gr						
к	10	100	500	1,000	5,000	10,000	
1	0.4182	0.8116	1.1400	1.3152	1.8147	2.2367	
1.1	0.3975	0.8352	1.1337	1.3094	1.8410	2.5195	
1.2	0.5098	0.8859	1.1904	1.3596	1.9184	2.5472	
1.3	0.5271	0.9232	1.2337	1.4018	1.9788	2.6212	
1.4	0.5393	0.9537	1.2691	1.4386	2.0291	2.6480	
1.5	0.5473	0.9797	1.3000	1.4708	2.0659	2.6003	
2	0.5598	1.0695	1.4164	1.6011	2.2430	2.7122	
5	0.4785	1.1902	1.6621	1.8939	2.5532	2.9352	
20	0.3076	1.1250	1.6981	1.9681	2.7312	3.1309	
50	0.2585	1.0711	1.6783	1.9557	2.7432	3.1581	
Straight channel	0.2267	1.0220	1.6589	1.9429	2.7462	3.1738	

Table 3. Average Nusselt number values over the hot curved wall of the channel

while moving over the hot wall, its temperature at a certain height is expected to increase, with a consequent decrease in Nu, as κ decreases. The relative influence of the aforementioned effects results in the Nu distributions presented in Figures 9c and 9d.

Further insight on heat transfer can be inferred from Table 3, which presents the average Nusselt number values for all the configurations studied. At a given κ value, \overline{Nu} increases with increasing Gr values because of the higher buoyancy effects. The effect of channel convexity on \overline{Nu} is not as clear. For $Gr \leq 10^2$, \overline{Nu} increases and then decreases as κ increases, with the maximum value occurring at $\kappa=2$ for Gr=10, and at $\kappa=5$ for Gr=100. For $500\leq Gr\leq 10^3$, variations in \overline{Nu} are very similar to the previously mentioned cases, with the maximum value being less apparent and very close to the straight channel value. For $Gr=5\times 10^3$, \overline{Nu} increases monotonically with κ . For $Gr=10^4$, a local minimum for \overline{Nu} is apparent within an overall increasing trend as κ increases. This \overline{Nu} distribution is due to the competing effects of pressure drop resulting from the channel expansion ratio, recirculation in the exit section, and curved wall length, as described above.

For $Gr \ge 100$, \overline{Nu} values displayed in Table 3 are correlated with a maximum absolute error less than 8.9% via the following equation:

$$\overline{Nu} = 0.4 \times Gr^{2/9} \left(1 + \frac{0.1}{\kappa} + \frac{0.8}{\kappa^2} \right)^{-1/2}$$
 (15)

To infer whether channels with convex walls increase or decrease the total heat transfer as compared to vertical channels with equal heated height, the average Nusselt number values are multiplied by the corresponding heated length of the channel, and the percent difference in the total heat transfer for the various cases studied are presented in Table 4. Values in the table are computed using

% difference =
$$100 \frac{(\overline{Nu} \times \ell)_{convex} - (\overline{Nu} \times \ell)_{straight}}{(\overline{Nu} \times \ell)_{straight}}$$
(16)

	Gr					
κ	10	100	500	1,000	5,000	10,000
1	189.77	24.74	7.95	6.33	3.80	10.70
1.1	120.09	2.58	-14.22	-15.41	-15.85	-0.36
1.2	165.84	2.47	-15.17	-17.28	-17.42	-5.13
1.3	165.28	3.06	-15.15	-17.68	-17.79	-5.77
1.4	164.97	3.94	-14.79	-17.53	-17.70	-7.07
1.5	164.26	4.93	-14.22	-17.14	-17.66	-10.32
2	158.59	9.59	-10.59	-13.70	-14.47	-10.51
5	112.50	17.25	0.87	-1.86	-6.40	-6.89
20	35.74	10.12	2.41	1.34	-0.50	-1.31
50	14.03	4.81	1.18	0.67	-0.10	-0.49

Table 4. Percent change in heat transfer compared to a straight channel of equal heated height

where

$$\begin{cases} \ell = H & \text{for } \kappa = \infty \\ \ell = H\kappa \sin^{-1}(1/\kappa) & \text{otherwise} \end{cases}$$
 (17)

As shown in Table 4, an increase in natural-convection heat transfer is obtained at all values of κ for $Gr \le 10^2$ and at all values of Gr for $\kappa = 1$. Moreover, estimates indicate a decrease in heat transfer for $5 \times 10^2 \le Gr \le 10^4$ and $1 < \kappa \le 2$.

CLOSING REMARKS

Laminar natural-convection heat transfer in convex channels was studied numerically. The flow dynamics are governed by the interplay of buoyancy forces arising from the temperature gradient and the opposing pressure gradient imposed by the expansion of the channel. At the smallest radius of curvature ($\kappa = 1$), results revealed the formation of two recirculation zones in the exit section of the channel at all Grashof number values. At a higher radius of curvature, only one recirculation zone was observed, and the value of Grashof numbers at which this recirculation occurred increased until it disappeared at κ values greater than 1.5. Recirculation zones appear for large Gr and small κ , due to the fact that the bulk of flow through the channel inlet follows the curved wall, which together with the opposing pressure gradient and the requirement of conservation of mass, forces one or more secondary flow at the ambient temperature to enter through the channel outlet. With smaller values of the expansion ratio and Grashof number, no recirculation zones were observed because the opposing pressure gradient does not overcome the buoyancy effects. The local Nusselt number along the channel decreases downstream as the component of the temperature gradient, normal to the channel wall, decreases (boundary-layer behavior). When recirculation zones exist and are strong enough to reach the diverging channel wall, an increase in Nusselt number is obvious. Because of the two opposing yet coupled effects of buoyancy and pressure gradient, there exists an optimum value for the channel radius of curvature to yield a maximum flow rate and a maximum average Nusselt number for a particular value of Grashof number. For all configurations, the calculated average Nusselt number (\overline{Nu}) values increased with increasing Grashof numbers. Channels with convex heated walls increased heat transfer at all values of κ for $Gr \leq 10^2$ and at all values of Gr for $\kappa=1,$ as compared to straight channels with equal heated heights.

REFERENCES

- 1. J. R. Bodia and J. F. Osterli, The Development of Free Convection between Heated Vertical Plates, *ASME J. Heat Transfer*, vol. 84, pp. 40–44, 1962.
- 2. W. Aung, L. S. Fletcher, and V. Sernas, Developing Laminar Free Convection between Vertical Flat Plates with Asymmetric Heating, *Int. J. Heat Mass Transfer*, vol. 15, pp. 2293–2308, 1972.
- 3. D. Naylor, J. M. Floryan, and J. D. Tarasuk, A Numerical Study of Developing Free Convection between Vertical Plates, *ASME J. Heat Transfer*, vol. 113, pp. 620–626, 1991.
- C. R. Maliska and F. Marcondes, Elliptic Calculations of Natural Convection Flows in Arbitrary Channels, Proc. 8th Int. Conf. on Laminar and Turbulent Flow, Swansea, UK, 1993
- 5. F. Marcondes and C. R. Maliska, Treatment of the Inlet Boundary Conditions in Natural-Convection Flows in Open-Ended Channels, *Numer. Heat Transfer B*, vol. 35, pp. 317–345, 1999.
- 6. W. Elenbaas, Heat Dissipation of Parallel Plates by Free Convection, *Physica*, vol. 9, pp. 1–28, 1942.
- E. M. Sparrow, G. M. Chrysler, and L. F. Azevedo, Observed Flow Reversals and Measured-Predicted Nusselt Numbers for Natural Convection in a One-Sided Heated Vertical Channel, ASME J. Heat Transfer, vol. 106, pp. 325–332, 1984.
- 8. A. O. Nieckle and L. F. A. Azevedo, Reverse Flow in One-Sided Heated Vertical Channels in Natural Convection, *Winter Annual Meeting of the ASME*, Boston, 1987, pp. 71–77.
- 9. S. E. Haaland and E. M. Sparrow, Solutions for the Channel Plume and the Parallel-Walled Chimney, *Numer. Heat Transfer*, vol. 6, pp. 155–172, 1983.
- 10. A. G. Straatman, J. D. Tarasuk, and J. M. Floryan, Heat Transfer Enhancement from a Vertical, Isothermal Channel Generated by the Chimney Effect, *ASME J. Heat Transfer*, vol. 115, pp. 395–402, 1993.
- 11. T. S. Fisher and K. E. Torrance, Experiments on Chimney-Enhanced Free Convection, *ASME J. Heat Transfer*, vol. 121, pp. 603–609, 1999.
- 12. A. Auletta, O. Manca, B. Morrone, and V. Naso, Heat Transfer Enhancement by the Chimney Effect in a Vertical Isoflux Channel, *Int. J. Heat Mass Transfer*, vol. 44, pp. 4345–4357, 2001.
- 13. O. Manca, M. Musto, and V. Naso, Experimental Analysis of Asymmetrical Isoflux Channel-Chimney Systems, *Int. J. Thermal Sci.*, vol. 42, pp. 837–846, 2003.
- 14. O. Manca, M. Musto, and V. Naso, Experimental Analysis of Chimney Effect in a Vertical Isoflux Channel, *Proc. 5th World Conf. on Experimental Heat Transfer, Fluid Dynamics, and Thermodynamics*, pp. 645–650, Thessaloniki, Greece, 2001.
- 15. A. Auletta, and O. Manca, Heat and Fluid Flow Resulting from the Chimney Effect in a Symmetrically Heated Channel with Adiabatic Extensions, *Int. J. Thermal Sci.*, vol. 41, pp. 1101–1111, 2002.
- 16. O. Manca, M. Musto, and V. Naso, Experimental Investigation of Natural Convection in an Asymmetrically Heated Vertical Channel with an Asymmetric Chimney, *ASME J. Heat Transfer*, vol. 127, pp. 888–896, 2005.

- 17. I. Pop and H. S. Takhar, Free Convection from a Curved Surface, *J. Appl. Math. Mech.* (ZAMM), vol. 73, pp. 534–539, 1993.
- 18. E. Magyari, I. Pop, and B. Keller, A Note on the Free Convection from Curved Surfaces, J. Appl. Math. Mech. (ZAMM), vol. 82, pp. 142–144, 2002.
- 19. A. Nakayama, H. Koyoma, and F. Kuwahara, Similarity Solution for Non-Darcy Free Convection from a Non-isothermal Curved Surface in a Fluid-Saturated Porous Medium, *J. Heat Transfer*, vol. 111, pp. 807–811, 1989.
- 20. M.-C. Char and C.-L. Chang, Laminar Free Convection Flow of Mircopolar Fluids from a Curved Surface, *J. Phys. D: Appl. Phys.*, vol. 28, pp. 1324–1331, 1995.
- 21. F. Moukalled, A. Doughan, and S. Acharya, Mixed-Convection Heat Transfer in Concave and Convex Channels, *AIAA J. Thermophys. Heat Transfer*, vol. 13, pp. 508–516, 1999.
- 22. F. Moukalled, A. Doughan, and S. Acharya, Parametric Study of Mixed Convection in Channels with Concave and Convex Surfaces, *Int. J. Heat Mass Transfer*, vol. 43, pp. 1947–1963, 2000.
- 23. G. K. Batchelor, *An introduction to Fluid Dynamics*, Cambridge University Press, London, UK, 1967.
- M. Peric, A Finite Volume Method for the Prediction of Three Dimensional Fluid Flow in Complex Ducts, Ph.D. thesis, Mechanical Engineering Department, Imperial College, London, 1985.
- 25. S. V. Patankar, Numerical Heat Transfer and Fluid Flow, Hemisphere, New York, 1980.
- 26. F. Moukalled and M. Darwish, Pressure Based Algorithms for Single and Multifluid Flow, in W. J. Minkowycz, E. M. Sparrow, and J. Y. Murthy (eds.), *Handbook of Numerical Heat Transfer*, 2nd ed., pp. 325–367, Wiley, New York, 2006.
- 27. F. Moukalled and M. Darwish, A Unified Formulation of the Segregated Class of Algorithms for Fluid Flow at All Speeds, *Numer. Heat Transfer B*, vol. 37, pp. 103–139, 2000.
- 28. P. J. Zwart, G. D. Raithby, and M. J. Raw, An Integrated Space-Time Finite-Volume Method for Moving-Boundary Problems, *Numer. Heat Transfer B*, vol. 34, pp. 257–270, 1998
- 29. P. H. Gaskell and A. K. C. Lau, Curvature Compensated Convective Transport: SMART, a New Boundedness Preserving Transport Algorithm, *Int. J. Numer. Meth. Fluids*, vol. 8, pp. 617–641, 1988.
- 30. M. Darwish and F. Moukalled, Normalized Variable and Space Formulation Methodology for High-Resolution Schemes, *Numer. Heat Transfer B*, vol. 26, pp. 79–96, 1994.
- 31. W. J. Gordon and L. C. Theil, Transfinite Mappings and Their Applications to Grid Generation, in J. F. Thompson (ed.), *Numerical Grid Generation*, pp. 171–192, North Holland, New York, 1982.
- 32. R. A. Wirtz and T. Haag, Effect of an Unheated Entry on Natural Convection between Vertical Parallel Plates, ASME Paper 85-WA/HT-14, 1985.